ARTICLE

Exciton Generation and Diffusion in Multilayered Organic Solar Cells Designed by Layer-by-Layer Assembly of Poly(*p*-phenylenevinylene)

Kohji Masuda, Yoshifumi Ikeda, Michihiro Ogawa, Hiroaki Benten, Hideo Ohkita,* and Shinzaburo Ito

Department of Polymer Chemistry, Graduate School of Engineering, Kyoto University, Katsura, Nishikyo, Kyoto 615-8510, Japan

ABSTRACT Solution-processed organic thin-film solar cells with triple-layered structures were fabricated by combining a hole-transporting layer made of poly(3,4-ethylenedioxythiophene):poly(4-styrenesulfonate) (PEDOT:PSS), a light-harvesting layer assembled by layer-by-layer (LbL) deposition of poly(*p*-phenylenevinylene) (PPV) and PSS, and an electron-transporting layer of fullerene C_{60} dispersed in a polystyrene film. The thickness of the light-harvesting layer was precisely designed and controlled on a scale of nanometers by the LbL deposition technique. The efficiency of exciton generation in the PPV/PSS LbL assembly was estimated for various layered structures by optical simulation considering optical interference effects. For the discussion on the efficiency of exciton diffusion, photoluminescence quenching was measured for the LbL assembly with various thicknesses and analyzed using the one-dimensional diffusion model. As a result, the exciton lifetime and diffusion constant were evaluated as 0.67 ± 0.02 ns and 8×10^{-4} $cm^2\ s^{-1}$, respectively. On the basis of these analyses, the photocurrent generation in the solar cells was quantitatively explained in terms of the layered structure.

KEYWORDS: exciton generation • exciton diffusion • poly(*p*-phenylenevinylene) • layer-by-layer assembly • organic solar cell

INTRODUCTION

Bulk-heterojunction polymer-based solar cells and planar-heterojunction small-molecule-based solar cells are representatives of organic thin-film solar cells (1). The power conversion efficiency has been reported to be around 5−6% for both devices (2–5). The former solar cells are typically fabricated by solution processes such as spin coating of a blend solution of a conjugated polymer and a fullerene derivative (6) and therefore have attracted much attention because of their suitability for high-throughput production based on the printing and coating techniques (7). On the other hand, the latter solar cells are typically fabricated by vacuum deposition of small molecules such as copper phthalocyanine and fullerene (4, 5, 8). One of the most remarkable advantages for such devices is that layered structures are precisely designed and controlled on a scale of subnanometers by the vacuum deposition technique (9). Such a precisely controlled device structure is beneficial not only for developing high-performance solar cells (4) but also for understanding a series of fundamental processes such as exciton generation, exciton diffusion, charge generation, and charge collection at the electrodes (8, 10). The photon absorption efficiency in well-ordered multilayered devices can be estimated by optical simulations considering optical interference effects (8). The efficiency of exciton diffusion to a donor/acceptor interface can be evaluated from photoluminescence (PL) quenching experiments using the one-dimensional diffusion model (8, 11, 12). A series of device analyses have been reported for small-molecule thin-film solar cells fabricated by vacuum deposition (8) and clearly provide a guideline for the design of more efficient solar cells.

To integrate both advantages of the solution processing and vacuum deposition techniques, we have developed multilayered organic thin-film solar cells fabricated by a combination of the spin-coating and layer-by-layer (LbL) deposition techniques. This technique, which was developed by Decher and Hong (13), is a simple and versatile method for fabricating ultrathin films (14) and is therefore applied to various ultrathin-film-coated applied materials (15) such as core−shell nanoparticles (16), two- or three-dimensional patterned structures (17) with a precisely controlled thickness on a scale of nanometers. Ultrathin films of poly(*p*-phenylenevinylene) (PPV) have been fabricated by the LbL deposition technique using a precursor of PPV (18) and then applied to organic thin-film solar cells (19). We previously designed the configuration of the light-harvesting layer in multilayered organic thin-film solar cells (11, 20–23). As a result of such structural optimization, we obtained the best-performance device with a power conversion efficiency of 0.26% under AM1.5G solar-simulated illumination. This efficiency is significantly higher than that reported for LbL-based organic solar cells (24–26). In the present study, we

* Corresponding author. E-mail: ohkita@photo.polym.kyoto-u.ac.jp.
Received for review October 1, 2009 and accepted December 17, 2009

DOI: 10.1021/am900660n

Published on Web 01/04/2010

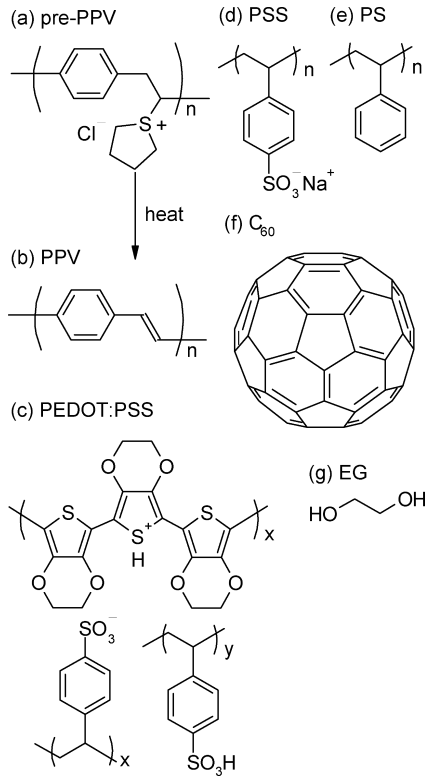

FIGURE 1. Chemical structures of materials used in this study.

discuss the relationship between the device efficiency and the device structure of LbL-based multilayered solar cells. Exciton generation in the LbL assembly is estimated by optical simulation. Exciton diffusion into a donor/acceptor interface is evaluated from the PL quenching experiments using the one-dimensional diffusion model. We demonstrate that the device performance can be quantitatively analyzed on the basis of a layered structure.

EXPERIMENTAL METHODS

Materials. Poly(*p*-xylenetetrahydrothiophenium chloride) (pre-PPV; Aldrich, 0.25 wt % aqueous solution) was diluted to 1 mM with ultrapure water. The solution was adjusted to pH 8−9 with a NaOH aqueous solution. The 1 mM pre-PPV aqueous solution was used as a cationic polyelectrolyte solution for the LbL deposition. Poly(sodium 4-styrenesulfonate) (PSS; Aldrich, M_w = 70 000 g mol^{-1}) was dissolved in ultrapure water to give a 10 mM PSS aqueous solution, which was used as an anionic polyelectrolyte solution for LbL deposition. Poly(3,4-ethylenedioxythiophene):poly(4-styrenesulfonate) (PEDOT:PSS; Aldrich, 1.3 wt % dispersion in water, conductive grade) was mixed with ethylene glycol (EG; Aldrich, anhydrous, 99.8%) (PEDOT:PSS/EG = 100/20 by weight). The mixed solution of PEDOT:PSS with EG was used for the fabrication of a hole-transporting layer by spin coating. Polystyrene (PS; Aldrich, M_w = 280 000 g mol^{-1}) was purified by reprecipitation from a toluene solution into methanol three times. To 2 mL of *o*-dichlorobenzene (Aldrich) was added 12 mg of PS and 48 mg of C_{60} (Frontier Carbon Co. Ltd.). The blend solution of PS and C_{60} was used for the fabrication of an electron-transporting layer by spin coating. Figure 1 shows the chemical structures of materials used in this study.

Device Fabrication. Indium−tin oxide (ITO)-coated glass substrates (10 Ω □$^{-1}$) were washed by ultrasonication in toluene, acetone, and ethanol for 15 min, respectively, and then dried with a N_2 flow. These prewashed substrates were further treated with a UV−O_3 cleaner for 1 h. First, a hole-transporting layer of PEDOT:PSS was prepared by spin coating from the aqueous solution of PEDOT:PSS mixed with EG and was thermally annealed at 70 °C for 14 h in air and at 140 °C for 1 h under vacuum to give an insoluble film as reported previously (21). The thickness of the PEDOT:PSS layer was ∼80 nm. Second, a light-harvesting layer was prepared by the LbL deposition of pre-PPV and PSS. The PEDOT:PSS-coated substrate was immersed in the 1 mM pre-PPV aqueous solution for 5 min, rinsed in ultrapure water for 3 min, immersed in the 10 mM PSS aqueous solution for 5 min, and rinsed in ultrapure water for 3 min. This cycle gives one bilayer of pre-PPV and PSS, which is abbreviated as (pre-PPV/PSS)$_1$. Each LbL film was completely dried under a flow of air for 4−6 min after the immersion. Third, an electron-transporting layer was prepared on n + 0.5 bilayers of pre-PPV/PSS, which is abbreviated as (pre-PPV/PSS)$_n$/pre-PPV, by spin coating from the *o*-chlorobenzene solution of C_{60} and PS. Subsequently, the (pre-PPV/PSS)$_n$/pre-PPV LbL assembly was thermally converted to the (PPV/PSS)$_n$/PPV LbL assembly by annealing at 100 °C for 2 h under vacuum. Finally, aluminum was thermally deposited as a counter electrode at 2.5 × 10^{-6} Torr on top of the triple-layered film through a metal mask to give an active area of 6 mm^2 (2 × 3 mm^2). The triple-layered device consisted of a hole-transporting layer of the PEDOT:PSS film, a light-harvesting layer of the PPV/PSS LbL film, and an electron-transporting layer of the C_{60}:PS film. The device structure is abbreviated as ITO|PEDOT:PSS|(PPV/PSS)$_n$/PPV|C_{60}:PS|Al. The thickness of the (PPV/PSS)$_n$/PPV light-harvesting layer was varied between 3 and 19 nm depending on the number of deposition cycles n. The detailed structural analysis of the device was described in ref 21. The thickness of the C_{60}:PS electron-transporting layer was varied between 20 and 50 nm by adjusting the spin rate.

Sample Preparation for the Quenching Experiment. Quartz substrates were washed by ultrasonication in toluene, acetone, and ethanol for 15 min, respectively, and then dried with a N_2 flow. These prewashed substrates were further treated with a UV−O_3 cleaner for 1 h. An emission layer of (pre-PPV/PSS)$_n$/pre-PPV was prepared on a quartz substrate by the same fabrication procedures as those described above. Before the thermal conversion of pre-PPV into PPV, a quenching layer was prepared on the (pre-PPV/PSS)$_n$/pre-PPV layer mentioned above by spin coating from the *o*-chlorobenzene solution of C_{60} and PS. As a control, a PS layer was prepared on the (pre-PPV/PSS)$_n$/pre-PPV layer by spin coating from the *o*-chlorobenzene solution of PS. Finally, the (pre-PPV/PSS)$_n$/pre-PPV LbL assembly was thermally converted to the (PPV/PSS)$_n$/PPV LbL assembly by annealing at 100 °C for 2 h under vacuum. The schematic layered structures of the PPV/PSS LbL films are shown in Figure 2, and the detailed characterization of the layered structures including each layer thickness is described in the Supporting Information.

Measurements. The current density−voltage (J−V) characteristics of the triple-layered devices of ITO|PEDOT:PSS|(PPV/PSS)$_n$/PPV|C_{60}:PS|Al were measured with a direct-current voltage current source/monitor (Advantest R6243) in the dark and under AM1.5G solar-simulated illumination at 100 mW cm^{-2}. The external quantum efficiency (EQE) was measured with a digital electrometer (Advantest R8252) under monochromatic light illumination at 420 nm from a 500 W xenon lamp (Thermo Oriel model 66921) with optical cut filters and a monochromator (Thermo Oriel, UV−visible Conerstone). Fluorescence spectra of the double-layered films of (PPV/PSS)$_n$/PPV|C_{60}:PS and (PPV/PSS)$_n$/PPV|PS on quartz substrates were measured with a fluorescence spectrometer (Hitachi F-4500). The excitation wavelength was 420 nm. The fluorescence decay of the double-layered films was measured by the time-correlated single-photon-counting method as described elsewhere (27, 28). The

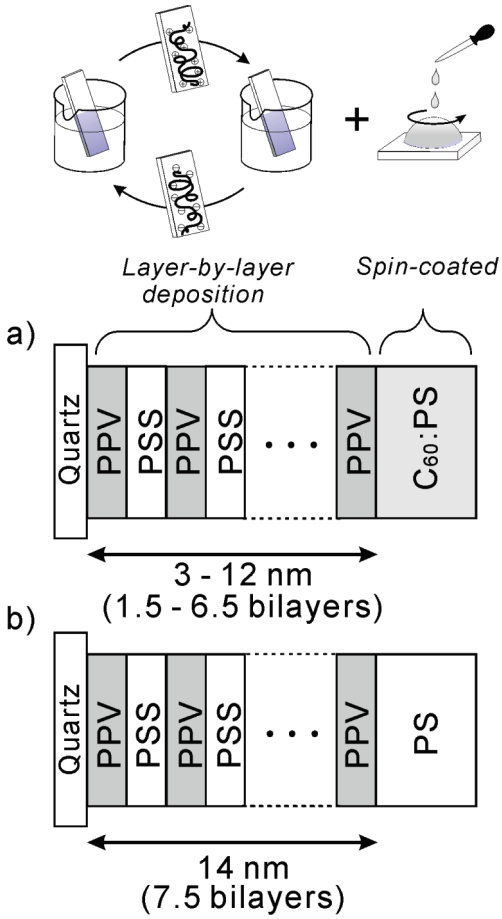

FIGURE 2. Schematic layered structures of the double-layered films employed for the quenching measurements: (a) (PPV/PSS)$_n$/PPV|C$_{60}$:PS; (b) (PPV/PSS)$_n$/PPV|PS. The monolayer thickness in (PPV/PSS)$_n$/PPV was 0.9 nm for PPV and 1.0 nm for PSS.

Table 1. Optical Parameters and Thicknesses of Each Component at 420 nm Employed for Calculation by the Transfer Matrix

component	n	k	thickness/nm	ref
glass	1.53	0	1.0×10^6	21
ITO	1.94	0.01	200	22
PEDOT:PSS	1.42	0.02	80	22
PPV	2.10	1.10	3−19	23
PSS	1.51	0	3−19	24
C$_{60}$:PS	2.05	0.20	20−50	25
Al	0.59	4.30	50	26

excitation wavelength was 440 nm. All of these measurements were performed in air at room temperature.

Optical Simulations. The photon absorption efficiency of the PPV/PSS LbL assembly is evaluated by the transfer matrix method (8, 29). For simplicity, we assume that each layer j (j = 1, 2, ..., m) consists of homogeneous and isotropic materials with a thickness L_j and a complex refractive index $\mathbf{n}_j = n_j + ik_j$. Furthermore, the interfaces are assumed to be optically flat even in the PPV/PSS LbL assembly, although there is a little interpenetration between neighboring LbL assemblies. The optical electric field amplitude $\mathbf{E}_j(x)$ is calculated as a function of the position in the multilayer structure in the thin film, where x is the position in layer j; $0 \le x \le L_j$. Here, $|\mathbf{E}_j(x)|^2$ is normalized by $|\mathbf{E}_0|^2$, where $\mathbf{E}_0$ is the optical electric field amplitude of the incident plane wave. The time average of the energy dissipated per second at position x in layer j, $Q_j(x)$, is then

$$Q_j(x) = \frac{1}{2} c\varepsilon_0 \alpha_j n_j |\mathbf{E}_j(x)|^2 \quad (1)$$

where c is the speed of light, ε_0 is the permittivity of free space, and α_j is the absorption coefficient of layer j. The exciton generation rate at position x in layer j is therefore given by $G_j(x) = (\lambda/hc)Q_j(x)$, where λ is the wavelength of the incident light and h is Planck's constant. Consequently, the absorption efficiency of the PPV/PSS LbL assembly is given by

$$\eta_A^{\mathrm{LbL}} = \sum_j^{\mathrm{LbL}} \int_0^{L_j} G_j(x)\, dx \quad (2)$$

In the same way, the absorption efficiency of the C$_{60}$:PS layer η_A^{C60} is also evaluated. Table 1 summarizes the optical parameters (30–35) and the thickness for each component employed for calculation by the transfer matrix.

RESULTS

Photocurrent Generation. To examine the relationship between photocurrent generation and the device structure, we fabricated various triple-layered polymer solar cells of ITO|PEDOT:PSS|(PPV/PSS)$_n$/PPV|C$_{60}$:PS|Al with different layer thicknesses. The thickness of the PPV/PSS LbL assembly was varied between 3 and 19 nm, and the thickness of the C$_{60}$:PS layer was varied between 20 and 50 nm. Figure 3a shows the dependence of the short-circuit current density J_{SC} and EQE of the solar cell on the thickness of the PPV/PSS LbL film. Note that the thickness of the C$_{60}$:PS layer was fixed at 30 nm. With an increase in the thickness of the PPV/PSS LbL film, as shown by the open circles in the figure, J_{SC} increased steeply by a factor of 2 from 3 to 7 nm, reached a maximum at around 7 nm, and then gradually decreased above it. As shown in the figure, EQE at 420 nm also showed the same tendency as J_{SC}. This trend is consistent with our previous report (21). The increase in J_{SC} below 7 nm is simply ascribed to the increase in the light-harvesting PPV/PSS LbL assembly, which increases the photon absorption efficiency η_A, leading to exciton generation. To explain the gradual decrease in J_{SC} above 7 nm, however, we should consider other limiting factors such as the efficiency of exciton diffusion to a donor/acceptor interface η_{ED} as discussed later. On the other hand, Figure 3b shows the dependence of J_{SC} of the solar cell on the thickness of the C$_{60}$:PS film. Note that the thickness of the PPV/PSS LbL assembly was fixed at 7 nm. As shown by the open circles in the figure, J_{SC} increased with an increase in the thickness of the C$_{60}$:PS film, decreased above 30 nm, and reduced by half at 50 nm even though the thickness of the light-harvesting PPV/PSS LbL assembly was kept constant. Thus, as described below, the optical interference effect should be taken into account in the photon absorption efficiency η_A in the device with a reflective metal mirror as an electrode.

Optical Simulation. To evaluate the photon absorption efficiency η_A, we calculate the internal optical electric field $\mathbf{E}(x)$ and the exciton generation rate $G(x)$ as a function of the position x in the multilayered organic solar cells by

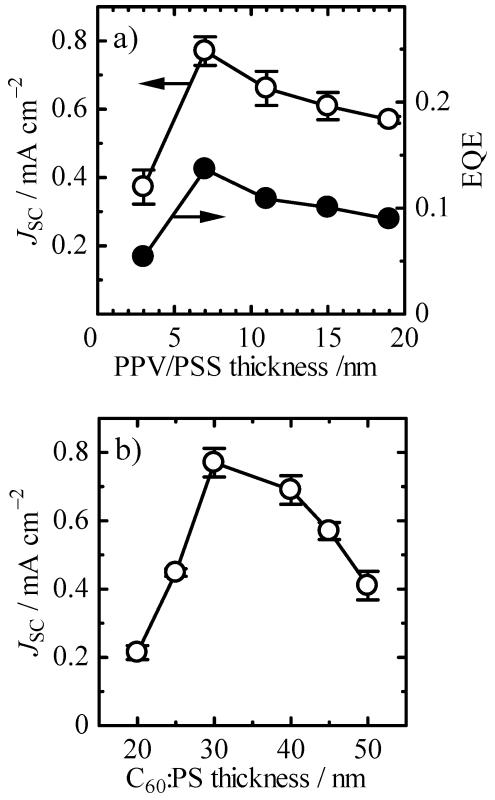

FIGURE 3. (a) Dependence of J_{SC} (open circles) and EQE at 420 nm (closed circles) on the thickness of the (PPV/PSS)$_n$/PPV layer measured for triple-layered devices of ITO|PEDOT:PSS|(PPV/PSS)$_n$/PPV (3−19 nm)|C_{60}:PS (30 nm)|Al, under AM1.5G solar-simulated illumination at 100 mW cm^{-1}. (b) Dependence of J_{SC} on the thickness of the C_{60}:PS layer measured for triple-layered devices of ITO|PEDOT:PSS|(PPV/PSS)$_n$/PPV (7 nm)|C_{60}:PS (20−50 nm)|Al, under AM1.5G solar-simulated illumination at 100 mW cm^{-1}. The experimental error in EQE was as small as 5%, and the error bars were within the closed circles.

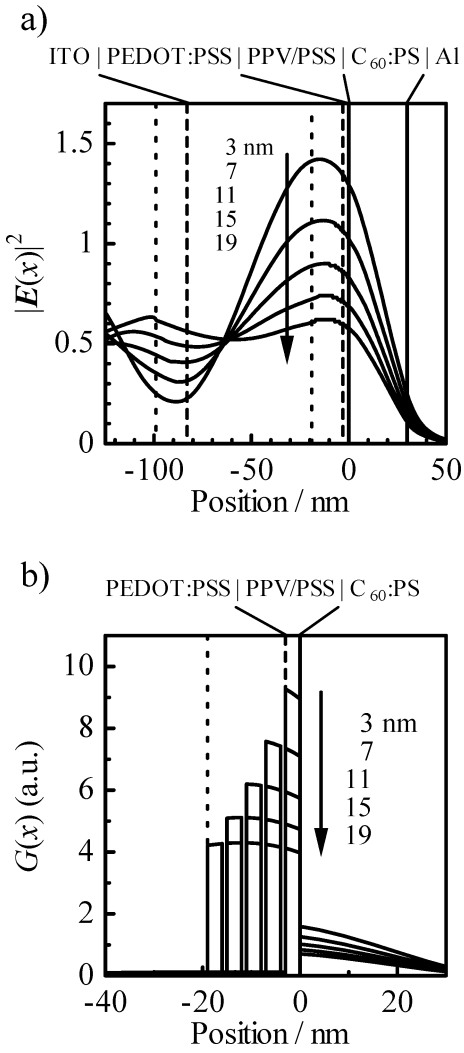

FIGURE 4. (a) Calculated distribution of the optical intensity $|\mathbf{E}(x)|^2$, which is normalized by the optical intensity of the incident plane wave. (b) Calculated distribution of the exciton generation rate $G(x)$. The device structure employed for the calculation is ITO (200 nm)|PEDOT:PSS (80 nm)|(PPV/PSS)$_n$/PPV (3−19 nm)|C_{60}:PS (30 nm)|Al.

the transfer matrix method. Figure 4a shows the optical intensity $|\mathbf{E}(x)|^2$ in multilayered organic solar cells with the PPV/PSS LbL assembly differing in thickness: the device structure is ITO (200 nm)|PEDOT:PSS (80 nm)|(PPV/PSS)$_n$/PPV (3−19 nm)|C_{60}:PS (30 nm)|Al. As the thickness of the PPV/PSS LbL assembly is increased, the peak value of $|\mathbf{E}(x)|^2$ is decreased monotonically but the peak position is almost unchanged. The decrease in $|\mathbf{E}(x)|^2$ is mainly due to the absorption of the PPV/PSS LbL assembly, although there should be optical interference effects, as is discussed later. As a result, as shown in Figure 4b, $G(x)$ in the PPV/PSS LbL assembly also decreases monotonically with an increase in the thickness of the PPV/PSS LbL assembly. Note that the values of $G(x)$ are much larger than that in the C_{60}:PS layer, suggesting that the PPV/PSS LbL assembly has a crucial role in the light harvesting of the device.

Figure 5a shows the optical intensity $|\mathbf{E}(x)|^2$ in multilayered organic solar cells with the C_{60}:PS layer differing in thickness: the device structure is ITO (200 nm)|PEDOT:PSS (80 nm)|(PPV/PSS)$_n$/PPV (7 nm)|C_{60}:PS (20−50 nm)|Al. As is the case with the PPV/PSS LbL assembly, the peak value of $|\mathbf{E}(x)|^2$ in the PPV/PSS LbL assembly decreases monotonically with an increase in the thickness of the C_{60}:PS layer. This decrease in $|\mathbf{E}(x)|^2$ is mainly due to the absorption of the C_{60}:PS layer. In contrast to Figure 4a, the peak position is significantly shifted from the PEDOT:PSS layer through the PPV/PSS LbL assembly to the C_{60}:PS layer, suggesting that the C_{60}:PS layer serves as an optical spacer, as is discussed later. As a result, as shown in Figure 5b, the dependence of $G(x)$ on the thickness of the C_{60}:PS layer is a bit more complex. The average values of $G(x)$ in the PPV/PSS LbL assembly increase slightly from 20 to 30 nm and then decrease above 30 nm with an increase in the thickness of the C_{60}:PS LbL assembly.

On the basis of these calculations, we evaluate the photon absorption efficiency in the PPV/PSS LbL assembly η_A^{LbL} at 420 nm. As the thickness of the PPV/PSS LbL assembly is increased, as shown by the open squares in Figure 6a, η_A^{LbL} monotonically increases up to around 20 nm and then is almost saturated above 20 nm. The open circles represent the absorption of the PPV/PSS LbL assembly simply calculated from the absorbance of the film. The closed circles represent the absorption of the PPV/PSS LbL assembly calculated from twice the absorbance of the film considering the reflection at the aluminum electrode. Note that the

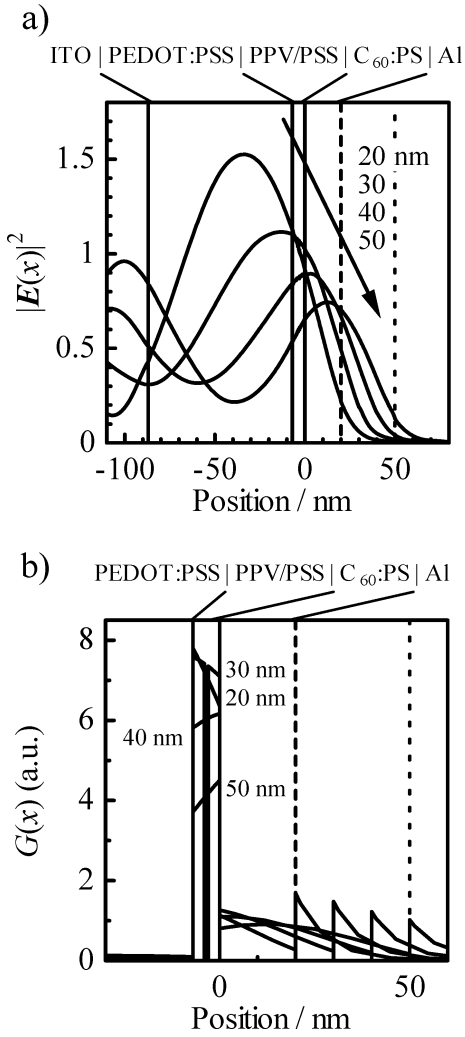

FIGURE 5. (a) Calculated distribution of the optical intensity $|E(x)|^2$, which is normalized by the optical intensity of the incident plane wave. (b) Calculated distribution of the exciton generation rate $G(x)$. The device structure employed for the calculation is ITO (200 nm)|PEDOT:PSS (80 nm)|$(PPV/PSS)_n$/PPV (7 nm)|C_{60}:PS (20−50 nm)|Al.

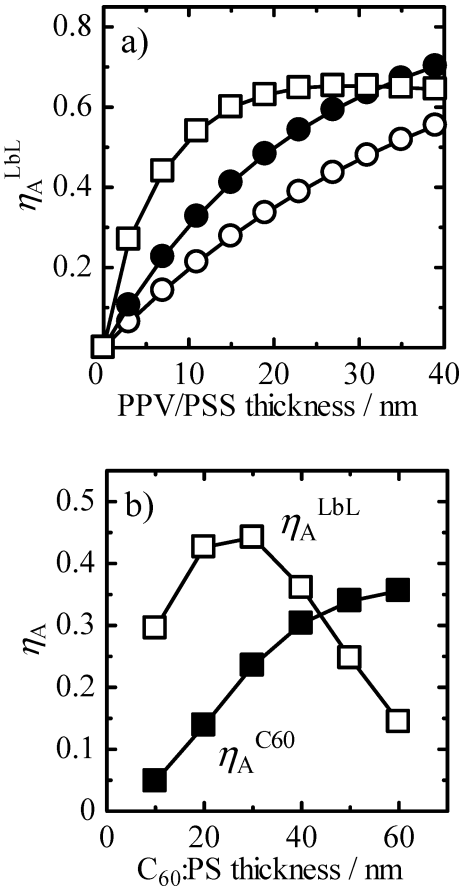

FIGURE 6. Photon absorption efficiency η_A^{LbL} in the PPV/PSS LbL assembly at 420 nm (open squares) plotted against the thickness of (a) the PPV/PSS LbL assembly and (b) the C_{60}:PS layer. The device structures are as follows: (a) ITO (200 nm)|PEDOT:PSS (80 nm)|$(PPV/PSS)_n$/PPV (0−39 nm)|C_{60}:PS (30 nm)|Al and (b) ITO (200 nm)|PEDOT:PSS (80 nm)|$(PPV/PSS)_n$/PPV (7 nm)|C_{60}:PS (10−60 nm)|Al. The open circles represent the absorption of the PPV/PSS LbL assembly calculated from the absorbance of the film. The closed circles represent the absorption of the PPV/PSS LbL assembly calculated from twice the absorbance of the film considering the reflection at the aluminum electrode. The closed squares represent the photon absorption efficiency η_A^{C60} in the C_{60}:PS layer at 420 nm. Note that the absorption of other layers such as ITO, PEDOT:PSS, and C_{60}:PS layers is also taken into account in the calculation.

absorption of other layers such as ITO, PEDOT:PSS, and C_{60}:PS layers is also taken into account in the calculation. In other words, this is the maximum absorption without consideration of optical interference effects. Thus, the difference between the open squares η_A^{LbL} and the closed circles clearly demonstrates that the optical interference effects have a great impact on the photon absorption efficiency in multilayered devices. We note that the thickness dependence of η_A^{LbL} is not consistent with that of J_{SC} shown in Figure 3a. This disagreement suggests that there are other limiting factors for charge generation, as is discussed later. As the thickness of the C_{60}:PS LbL assembly is increased, on the other hand, η_A^{LbL} slightly increases from 20 to 30 nm and then decreases above 30 nm, while η_A^{C60} increases monotonically, as shown in Figure 6b. The thickness dependence of J_{SC} shown in Figure 3b is in good agreement with that of η_A^{LbL} rather than η_A^{C60}, suggesting that the contribution of the C_{60}:PS layer to photocurrent generation is negligibly minor and the PPV/PSS LbL assembly has a major role in the light harvesting. Therefore, we focus our attention on charge generation from excitons generated in the PPV/PSS LbL assembly in this study.

Exciton Quenching. As mentioned before, we cannot explain the dependence of J_{SC} on the thickness of the PPV/PSS LbL assembly in terms of the photon absorption efficiency of the LbL assembly η_A^{LbL} alone. This is partly because some excitons generated in the LbL assembly cannot reach a donor/acceptor interface. Here, we therefore evaluate the exciton diffusion efficiency η_{ED}, which is the probability that the photogenerated exciton diffuses to a donor/acceptor interface before deactivating to the ground state, from exciton quenching experiments. First we measured the PL spectra of double-layered films with different layered structures as shown in Figure 2a,b to evaluate the quenching efficiency qualitatively: $(PPV/PSS)_n$/PPV|C_{60}:PS films and $(PPV/PSS)_n$/PPV|PS reference films. The PL intensity is normalized by that of the reference film with the same PPV/PSS LbL film in thickness. The quenching efficiency Φ_q

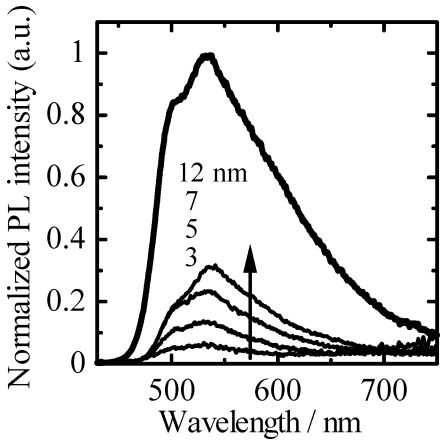

FIGURE 7. PL spectra of double-layered films with a layered structure of (PPV/PSS)$_n$/PPV (3−12 nm)|C$_{60}$:PS (solid lines) and the reference film with a layered structure of (PPV/PSS)$_7$/PPV (14 nm)|PS (thick solid line), as shown in parts a and b of Figure 2, respectively. The excitation wavelength was 420 nm. Each PL intensity of (PPV/PSS)$_n$/PPV|C$_{60}$:PS was normalized by that of the reference film with the same thickness of the PPV/PSS LbL film.

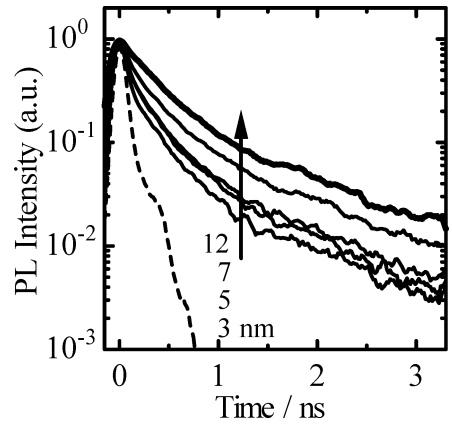

FIGURE 8. Fluorescence decay curves of double-layered films with a layered structure of (PPV/PSS)$_n$/PPV (3−12 nm)|C$_{60}$:PS (solid lines) and the reference film with a layered structure of (PPV/PSS)$_7$/PPV (14 nm)|PS (thick solid line), as shown in parts a and b of Figure 2, respectively. The excitation wavelength was 440 nm. The broken line represents the instrument response function (fwhw ∼ 60 ps).

is estimated by $1 - I/I_0$, where I is the PL intensity of the (PPV/PSS)$_n$/PPV|C$_{60}$:PS films and I_0 is that of the reference films. For the thinnest PPV/PSS LbL assembly, Φ_q was as high as 0.95, suggesting that almost all excitons are efficiently quenched at the quenching wall of the C$_{60}$:PS film. The quenching mechanism will be discussed later. As the thickness of the PPV/PSS LbL assembly is increased from 3 to 12 nm, the PL intensity increased as shown in Figure 7 and hence Φ_q decreased, suggesting that exciton quenching occurs only at a donor/acceptor interface and therefore some excitons cannot reach the interface as the thickness of the PPV/PSS LbL assembly is increased. Thus, we can discuss exciton diffusion by analyzing the dependence of Φ_q on the thickness of the PPV/PSS LbL assembly as described below.

To discuss the quenching efficiency quantitatively, we next measured the exciton lifetime by the time-correlated single-photon-counting method. This approach is more reliable than the PL intensity measurement because it is less sensitive to slight variations in the experimental conditions (36). Figure 8 shows the PL decay of double-layered films with different layered structures. The solid lines represent the PL decay of double-layered films with a layered structure of (PPV/PSS)$_n$/PPV (3−12 nm)|C$_{60}$:PS. The thick solid line represents the PL decay of a double-layered reference film with a layered structure of (PPV/PSS)$_n$/PPV (14 nm)|PS. The PL decays are well fitted by eq 3,

$$I(t) = I(0)\sum_i A_i \exp\left(-\frac{t}{\tau_i}\right) \tag{3}$$

where $I(t)$ and $I(0)$ are the PL intensity at time t and 0, respectively, A_i is the fraction of the ith component, and τ_i is the decay constant. The average PL lifetime $\langle\tau\rangle$ is calculated by eq 4 (12).

$$\langle\tau\rangle = \frac{\sum_i A_i \tau_i^2}{\sum_i A_i \tau_i} \tag{4}$$

The exciton lifetime in the PPV/PSS reference film is evaluated as $\langle\tau_0\rangle = 0.67 \pm 0.02$ ns, which is slightly longer than the previously reported values (37–39). On the other hand, the exciton lifetime in the PPV/PSS LbL films with the C$_{60}$:PS quenching layer was dependent on the thickness of the PPV/PSS LbL assembly; it increased from 0.40 ns at 5 nm to 0.63 ns at 12 nm with an experimental error of 2% at most. This tendency is qualitatively consistent with the PL quenching efficiency mentioned before. Furthermore, we can evaluate the quenching efficiency Φ_q by integrating eq 3. Table 2 summarizes the averaged exciton lifetime $\langle\tau\rangle$, other fitting parameters, and Φ_q. On the basis of these experimental quenching results, we will discuss later the diffusion constant of excitons in the PPV/PSS LbL assembly.

DISCUSSION

Exciton Generation. Exciton generation is proportional to the optical intensity in the light-harvesting layer. Thus, we first consider how the optical intensity depends on the layered structure of the device. As shown in Figures 4 and 5, the spatial distribution of the optical intensity $|\mathbf{E}(x)|^2$ in the multilayered device is significantly dependent on the thickness of the C$_{60}$:PS layer rather than that of the PPV/PSS LbL assembly. This is partly due to the relatively large refractive index of the C$_{60}$:PS layer, which extends the optical length effectively and hence shifts the peak position close to the electrode. This effect has been reported as the optical spacer effect (40, 41), which can enhance light absorption as a result of redistribution of the optical electric field for thin films but is less pronounced for thicker films (42). In our devices, the optical intensity $|\mathbf{E}(x)|^2$ in the LbL assembly is maximized with ∼30 nm of the C$_{60}$:PS layer, as shown in Figure 5a. Consequently, the photon absorption efficiency

Table 2. Fitting Parameters in Eq 3, $\langle\tau\rangle$, and Φ_q

L/nm	A_1 [a]	τ_1 [a]/ns	A_2 [a]	τ_2 [a]/ns	A_3 [a]	τ_3 [a]/ns	$\langle\tau\rangle$/ns	Φ_q [c]
3	0.86	0.02	0.12	0.21	0.02	1.10	0.40 ± 0.01	0.83
5	0.75	0.02	0.22	0.17	0.03	0.91	0.40 ± 0.01	0.78
7	0.75	0.05	0.21	0.24	0.04	1.11	0.45 ± 0.01	0.66
12	0.69	0.07	0.25	0.31	0.06	1.32	0.63 ± 0.01	0.46
14 [b]	0.84	0.23	0.16	1.16			0.67 ±0.02	

[a] The experimental error was within 2%. [b] Fitted with a sum of two exponential functions. [c] Evaluated by $1 - I/I_0$, where I and I_0 are calculated by the integration of eq 3 using fitting parameters.

leading to exciton generation in the LbL assembly η_A^{LbL} is also maximized with ~30 nm of the C_{60}:PS layer, as shown in Figure 6b. This trend is consistent with the dependence of J_{SC} on the thickness of the C_{60}:PS layer. If excitons generated in the C_{60}:PS layer mainly contributed to photocurrent generation, the dependence of J_{SC} on the thickness of the C_{60}:PS layer would follow that of η_A^{C60} considering a C_{60} exciton diffusion length as long as 40 nm (8). As shown in Figures 3b and 6b, this is not the case. Thus, we conclude that excitons generated in the LbL assembly mainly contribute to photocurrent generation. The negligibly minor contribution of C_{60} excitons to photocurrent generation is partly due to their rapid intersystem crossing to the triplet state as previously discussed (21). More importantly, it is noteworthy that the optical intensity in the light-harvesting layer can be maximized by optimization of the thickness of the C_{60}:PS layer. On the other hand, as mentioned before, the increase in the thickness of the PPV/PSS LbL assembly does not affect the spatial distribution of the optical intensity $|\mathbf{E}(x)|^2$ but simply decreases the intensity mainly because of absorption in the layer. As a result, as shown in Figure 6a, η_A^{LbL} increases monotonically with an increase in the thickness of the PPV/PSS LbL assembly and then is gradually saturated above 20 nm. Assuming that the reflection at the aluminum electrode is 100%, the optical length in the device would be twice as much and therefore the absorption could be estimated from twice the absorbance of the film. As shown in Figure 6a, η_A^{LbL} is larger for thinner LbL films (<30 nm) than the absorption calculated from twice the absorbance of the film but smaller for thicker LbL films (>30 nm). These results show that the photon absorption efficiency is enhanced for thinner LbL films (<30 nm) but is rather suppressed for thicker LbL films (>30 nm) by the optical interference effect. Consequently, no increase in η_A^{LbL} is expected above 20 nm even though the thickness of the LbL assembly increases. As shown in Figure 3a, such saturation is also seen in the dependence of J_{SC} on the thickness of the LbL assembly. Nonetheless, the optimized thickness of the LbL assembly is substantially different between η_A^{LbL} and J_{SC}. This discrepancy suggests that not all of the excitons generated in the LbL assembly can reach a donor/acceptor interface or contribute to the photocurrent generation. Thus, we will discuss the exciton diffusion efficiency η_{ED} in the next section.

Exciton Diffusion. We discuss the exciton diffusion in the PPV/PSS LbL film using the one-dimensional diffusion model in the direction normal to the substrate (11). Figure 9 shows a schematic illustration of the concentration profiles of the exciton in the PPV/PSS LbL film with a thickness of L, where the x axis is the direction normal to the substrate, the interface between the inert substrate and the PPV/PSS LbL film is located at $x = 0$, and the quenching surface of the C_{60}:PS film is located at $x = L$.

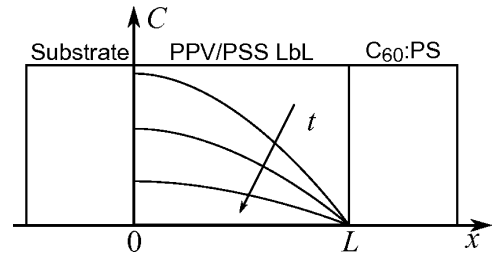

FIGURE 9. Schematic illustration of the time dependence of the concentration profiles $C(x,t)$ of PPV excitons in the PPV/PSS LbL film with a thickness of L, where the x axis is the direction normal to the substrate, the interface between the inert substrate and the PPV/PSS LbL film is located at $x = 0$, and the quenching surface of the C_{60}:PS film is located at $x = L$.

In this model, the concentration of the exciton $C(x,t)$ obeys Fick's law and can be expressed with a diffusion constant D by

$$\frac{\partial C(x,t)}{\partial t} = D\frac{\partial^2 C(x,t)}{\partial x^2} \tag{5}$$

As the initial condition, $C(x,0)$ is assumed to be constant throughout the film. This assumption is reasonable, as shown in Figure 4a, because the film is thin enough to be excited homogeneously.

$$C(x,0) = C_0 \tag{6}$$

As boundary conditions, it is assumed that all excitons arriving at $x = L$ are quenched by the C_{60}:PS layer. This is also reasonable because the quenching efficiency Φ_q is close to unity for the thinnest LbL assembly, as mentioned before. Thus, one of the boundary conditions is given by

$$C(L,t) = 0 \tag{7}$$

It is also assumed that all excitons arriving at $x = 0$ are just reflected to the opposite direction. Thus, the other boundary condition is given by

$$\left[\frac{\partial C(x,t)}{\partial x}\right]_{x=0} = 0 \tag{8}$$

With these boundary conditions, eq 5 can be analytically solved, and hence $C(x,t)$ is given by

$$C(x,t) = C_0 - C_0 \sum_{n=0}^{\infty} (-1)^n \left[\operatorname{erfc} \frac{(2n+1)L - x}{2\sqrt{Dt}} + \operatorname{erfc} \frac{(2n+1)L + x}{2\sqrt{Dt}} \right] \quad (9)$$

Consequently, we can calculate the quenching efficiency $\Phi_q(L,D)$ as a function of L and D.

$$\Phi_q(L,D) = 1 - \frac{I}{I_0} = 1 - \frac{\int_0^\infty I_0(t) \int_0^L C(x,t)\, dx\, dt}{\int_0^\infty I_0(t) \int_0^L C_0\, dx\, dt} \quad (10)$$

Figure 10 shows the quenching efficiency Φ_q evaluated by the PL decay (open circles) and the quenching efficiency $\Phi_q(L,D)$ predicted by eq 10 with several diffusion constants over 3 orders of magnitude (solid lines). As shown in the figure, the experimental quenching efficiencies Φ_q are close to one of the predicted lines $\Phi_q(L,D = 10^{-3}\ cm^2\ s^{-1})$. More precisely, they are well reproduced with an exciton diffusion constant of $D = 8 \times 10^{-4}\ cm^2\ s^{-1}$. Slight deviations seen for thinner PPV/PPS layers ($L < 5$ nm) are probably due to a static quenching, which is likely to be missed in the time-correlated single-photon-counting method. Indeed, the predicted $\Phi_q(L,D)$ is consistent with the PL quenching efficiency Φ_q as high as 0.95 observed for the thinnest PPV/PSS LbL assembly. As mentioned before, the exciton lifetime is $\langle\tau_0\rangle = 0.67$ ns. Therefore, the exciton diffusion length is estimated to be $(2D\langle\tau_0\rangle)^{1/2} = 10$ nm, which is slightly longer than previously reported values: The exciton diffusion length has been reported to be 5−8 nm for PPV and PPV derivatives (12, 36, 38, 43, 44). This is partly because the exciton lifetime in our PPV/PSS LbL film is longer than that in other reports for PPV and PPV derivatives (0.2−0.5 ns). The relatively longer exciton lifetime is consistent with the improved PL efficiency, as reported previously (20). We ascribed the improvement to the decrease in the trap-site concentration due to the low-temperature conversion of PPV. Therefore, we conclude that the long exciton diffusion is characteristic of PPV/PPS LbL films converted at a low temperature, which is beneficial for polymer-based solar cells (21).

Photon Conversion Efficiency. Finally, we discuss photocurrent generation in terms of EQE, which can be defined by eq 11 as the product of the efficiencies of four sequential steps: (1) the efficiency of photon absorption leading to the exciton generation η_A, (2) the efficiency of exciton diffusion to a donor/acceptor interface η_{ED}, (3) the efficiency of exciton dissociation by charge transfer at a donor/acceptor interface η_{CT}, and (4) the efficiency of charge collection of charge-separated carriers to the electrodes η_{CC}.

$$EQE = \eta_A \times \eta_{ED} \times \eta_{CT} \times \eta_{CC} \quad (11)$$

As described before, η_A was calculated by the transfer matrix method. We can evaluate η_{ED} as $\Phi_q = \eta_{ED} \times \eta_q \sim \eta_{ED}$ because the quenching efficiency at the interface η_q is almost unity, as mentioned before. Thus, η_{CT} can be assumed to be unity if the quenching mechanism is due to the charge transfer at a donor/acceptor interface. Another possible quenching mechanism is the energy transfer from PPV exciton to C_{60}, as reported previously (21). We roughly estimate the energy transfer rate based on the Förster theory assuming point dipoles to be $\sim 10^{12}\ s^{-1}$ for a PPV−C_{60} separation distance of 1 nm. This is 2 orders of magnitude less than the charge-transfer rate reported for PPV/PCBM blends (45). Thus, we conclude that quenching is mainly due to charge transfer at the donor/acceptor interface. Consequently, we can set $\eta_{CT} = 1$ for our multilayered organic solar cells. Therefore, η_{CC} can be estimated by eq 11 with η_A, η_{ED}, η_{CT}, and the experimental EQE values as shown in Figure 3a. Figure 11 summarizes the dependence of η_A, η_{ED}, η_{CC}, and EQE on the thickness of the PPV/PSS LbL film. As shown in the figure, η_{CC} is almost constant at around 0.5 above 7 nm in thickness. This indicates that half of the charges generated at the donor/acceptor interface can be collected at the electrodes under the short-circuit condition, which is consistent with our previous report (21). Possible loss mechanisms for η_{CC} are a rapid back recombination and an efficient bimolecular recombination in the film. On the basis of these efficiencies in each primary process, we conclude that EQE of our multilayered solar cells is optimized as a result of a balance between η_A and η_{ED}, which can be tuned by the precise thickness control of the LbL assembly on a scale of nanometers.

As described above, the device performance can be quantitatively explained by efficiencies in fundamental processes evaluated on the basis of the layered structure of the device. This is a great advantage for designing multilayered organic solar cells, as was already reported for small-molecule-based organic solar cells fabricated by dry processes such as vacuum deposition. In this study, we fabricated multilayered solar cells only by solution processes such as spin coating and LbL deposition techniques. This suggests that even solution-processed multilayered solar cells can be designed with a layered structure precisely controlled on a

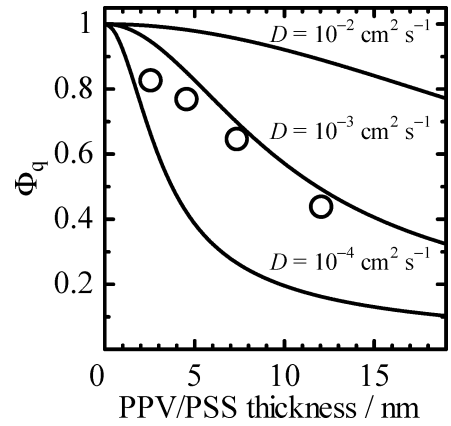

FIGURE 10. Dependence of Φ_q on the thickness of the PPV/PSS LbL film. The open circles represent Φ_q evaluated from the PL decays. The solid lines represent $\Phi_q(L,D)$ with different diffusion constants of $D = 10^{-2}$, 10^{-3}, and 10^{-4} cm^2 s^{-1}. The experimental error was as small as 2%, and the error bars were within the circles.

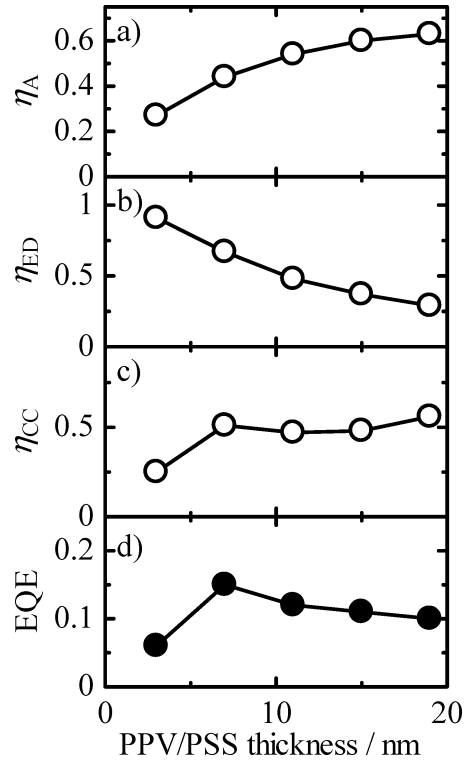

FIGURE 11. Dependence of each efficiency on the thickness of the PPV/PSS LbL film: (a) η_A is estimated by the transfer matrix method, (b) η_{ED} is evaluated from the PL quenching experiment, (c) η_{CC} is estimated from η_A, η_{ED}, and EQE, and (d) EQE at 420 nm is the same experimental data as shown in Figure 3a. The device structure is as follows: ITO (200 nm)|PEDOT:PSS (80 nm)|$(PPV/PSS)_n$/PPV (3−19 nm)|C_{60}:PS (30 nm)|Al. The experimental error of the data points in each efficiency was as small as 5%, and the error bars were within circles.

scale of nanometers by the LbL deposition technique, therefore, upon which the device performance can be optimized, as is the case with dry-processed small-molecule-based organic solar cells.

CONCLUSIONS

We fabricated all solution-processed organic thin-film solar cells consisting of a hole-transporting PEDOT:PSS layer, a light-harvesting PPV/PSS LbL assembly, and an electron-transporting C_{60}:PS layer. The thickness of the PPV/PSS LbL assembly was precisely varied between 3 and 19 nm on a scale of nanometers by the LbL deposition technique. The thickness of the C_{60}:PS layer was also varied between 20 and 50 nm by adjusting the spin rate. First, the photon absorption efficiency leading to exciton generation η_A in the light-harvesting LbL assembly was estimated for various device structures by the transfer matrix method. The η_A value was more sensitively dependent on the thickness of the C_{60}:PS layer than that of the PPV/PSS LbL assembly. Thus, we conclude that the C_{60}:PS layer serves as an effective optical spacer to enhance the optical intensity in the light-harvesting layer. Furthermore, η_A was enhanced for thinner LbL films (<30 nm) but rather suppressed for thicker LbL films (>30 nm) because of the optical interference effect. Second, the efficiency of exciton diffusion into a donor/acceptor interface η_{ED} was evaluated from the PL quenching experiments. The exciton lifetime was evaluated as 0.67 ± 0.02 ns by the PL decay measurement, which is slightly longer than the previously reported values. Using the one-dimensional diffusion model, we estimated the exciton diffusion constant to be 8×10^{-4} cm^2 s^{-1}, and the exciton diffusion length to be 10 nm, which is comparable to the optimized thickness of the PPV/PSS LbL assembly. Third, the efficiency of exciton dissociation by charge transfer at a donor/acceptor interface was assumed to be $\eta_{CT} \sim 1$ because the PL quenching was as high as 0.95 for the thinnest LbL film. Finally, the efficiency of charge collection to the electrodes η_{CC} was estimated to be ∼0.5 for the PPV/PSS LbL assembly with a thickness of >7 nm from η_A, η_{ED}, η_{CT}, η_{CC}, and experimentally obtained EQE values. These results demonstrate that the device performance can be quantitatively explained in terms of the device structure. Therefore, we can rationally improve the device performance by optimizing the device structure on the basis of these device analyses, which is a great advantage of multilayered organic thin-film solar cells as reported for small-molecule-based solar cells so far.

Acknowledgment. This work was partly supported by the Global COE program (International Center for Integrated Research and Advanced Education in Materials Science) and by the Integrative Industry−Academia Partnership (IIAP) project including Kyoto University, Hitachi, Ltd., and Mitsubishi Chemical Corp.

Supporting Information Available: Materials, fabrication, and characterization of PPV/PSS LbL films on a quartz substrate. This material is available free of charge via the Internet at http://pubs.acs.org.

REFERENCES AND NOTES

(1) Kippelen, B.; Brédas, J.-L. *Energy Environ. Sci.* **2009**, *2*, 251–261.
(2) Kim, J. Y.; Lee, K.; Coates, N. E.; Moses, D.; Nguyen, T.-Q.; Dante, M.; Heeger, A. J. *Science* **2007**, *317*, 222–225.
(3) Park, S. H.; Roy, A.; Beaupré, S.; Cho, S.; Coates, N.; Moon, J. S.; Moses, D.; Leclerc, M.; Lee, K.; Heeger, A. J. *Nat. Photonics* **2009**, *3*, 297–303.
(4) Xue, J.; Uchida, S.; Rand, B. P.; Forrest, S. R. *Appl. Phys. Lett.* **2004**, *85*, 5757–5759.
(5) Sakai, K.; Hiramoto, M. *Mol. Cryst. Liq. Cryst.* **2008**, *491*, 284–289.
(6) Dennler, G.; Scharber, M. C.; Brabec, C. J. *Adv. Mater.* **2009**, *21*, 1323–1338.
(7) Brabec, C. J.; Durrant, J. R. *MRS Bull.* **2008**, *33*, 670–675.
(8) Peumans, P.; Yakimov, A.; Forrest, S. R. *J. Appl. Phys.* **2003**, *93*, 3693–3723.
(9) Forrest, S. R. *Chem. Rev.* **1997**, *97*, 1793–1896.
(10) Yang, F.; Forrest, S. R. *ACS Nano* **2008**, *2*, 1022–1032.
(11) Fushimi, T.; Oda, A.; Ohkita, H.; Ito, S. *J. Phys. Chem. B* **2004**, *108*, 18897–18902.
(12) Markov, D. E.; Hummelen, J. C.; Blom, P. W. M. *Phys. Rev. B: Condens. Matter* **2005**, *72*, 045216.
(13) Decher, G.; Hong, J. D. *Makromol. Chem. Macromol. Symp.* **1991**, *46*, 321–327.
(14) Decher, G. *Science* **1997**, *277*, 1232–1237.
(15) Ariga, K.; Hill, J. P.; Ji, Q. *Phys. Chem. Chem. Phys.* **2007**, *9*, 2319–2340.
(16) Caruso, F. *Adv. Mater.* **2001**, *13*, 11–22.
(17) Hammond, P. T. *Adv. Mater.* **2004**, *16*, 1271–1293.
(18) Ferreira, M.; Cheung, J. H.; Rubner, M. F. *Thin Solid Films* **1994**, *244*, 806–809.
(19) Mattoussi, H.; Rubner, M. F.; Zhou, F.; Kumar, J.; Tripathy, S. K.; Chiang, L. Y. *Appl. Phys. Lett.* **2000**, *77*, 1540–1542.
(20) Ogawa, M.; Kudo, N.; Ohkita, H.; Ito, S.; Benten, H. *Appl. Phys. Lett.* **2007**, *90*, 223107.

(21) Benten, H.; Ogawa, M.; Ohkita, H.; Ito, S. *Adv. Funct. Mater.* **2008**, *18*, 1563–1572.
(22) Benten, H.; Kudo, N.; Ohkita, H.; Ito, S. *Thin Solid Films* **2009**, *517*, 2016–2022.
(23) Ogawa, M.; Tamanoi, M.; Ohkita, H.; Benten, H.; Ito, S. *Sol. Energy Mater. Sol. Cells* **2009**, *93*, 369–374.
(24) Mwaura, J. K.; Pinto, M. R.; Witker, D.; Ananthakrishnan, N.; Schanze, K. S.; Reynolds, J. R. *Langmuir* **2005**, *21*, 10119–10126.
(25) Durstock, M. F.; Spry, R. J.; Baur, J. W.; Taylor, B. E.; Chiang, L. Y. *J. Appl. Phys.* **2003**, *94*, 3253–3259.
(26) Li, H.; Li, Y.; Zhai, J.; Cui, G.; Liu, H.; Xiao, S.; Liu, Y.; Lu, F.; Jiang, L.; Zhu, D. *Chem.—Eur. J.* **2003**, *9*, 6031–6038.
(27) Benten, H.; Guo, J.; Ohkita, H.; Ito, S.; Yamamoto, M.; Sakumoto, N.; Hori, K.; Tohda, Y.; Tani, K. *J. Phys. Chem. B* **2007**, *111*, 10905–10914.
(28) Ohkita, H.; Benten, H.; Anada, A.; Noguchi, H.; Kido, N.; Ito, S.; Yamamoto, M. *Phys. Chem. Chem. Phys.* **2004**, *6*, 3977–3984.
(29) Pettersson, L. A. A.; Roman, L. S.; Inganäs, O. *J. Appl. Phys.* **1999**, *86*, 487–496.
(30) *Handbook of Chemistry and Physics*, 68th ed.; Weast, R. C., Astle, M. J., Beyer, W. H., Eds.; The Chemical Rubber Co.: Cleveland, OH, 1987; p E-372.
(31) Dennler, G.; Forberich, K.; Scharber, M. C.; Brabec, C. J.; Tomiš, I.; Hingerl, K.; Fromherz, T. *J. Appl. Phys.* **2007**, *102*, 054516.
(32) Kumar, S.; Biswas, A. K.; Shukla, V. K.; Awasthi, A.; Anand, R. S.; Narain, J. *Synth. Met.* **2003**, *139*, 751–753.
(33) Liu, L.; Li, P.; Asher, S. A. *J. Am. Chem. Soc.* **1999**, *121*, 4040–4046.
(34) These values were calculated by averaging as the volume fraction between C_{60} and PS.
(35) Lehmuskero, A.; Kuittinen, M.; Vahimaa, P. *Opt. Express* **2007**, *15*, 10744–10752.
(36) Markov, D. E.; Amsterdam, E.; Blom, P. W. M.; Sieval, A. B.; Hummelen, J. C. *J. Phys. Chem. A* **2005**, *109*, 5266–5274.
(37) Samuel, I. D. W.; Crystall, B.; Rumbles, G.; Burn, P. L.; Holmes, A. B.; Friend, R. H. *Chem. Phys. Lett.* **1993**, *213*, 472–478.
(38) Lewis, A. J.; Ruseckas, A.; Gaudin, O. P. M.; Webster, G. R.; Burn, P. L.; Samuel, I. D. W. *Org. Electron.* **2006**, *7*, 452–456.
(39) Smilowitz, L.; Hays, A.; Heeger, A. J.; Wang, G.; Bowers, J. E. *J. Chem. Phys.* **1993**, *98*, 6504–6509.
(40) Hänsel, H.; Zettl, H.; Krausch, G.; Kisselev, R.; Thelakkat, M.; Schmidt, H.-W. *Adv. Mater.* **2003**, *15*, 2056–2060.
(41) Kim, J. Y.; Kim, S. H.; Lee, H.-H.; Lee, K.; Ma, W.; Gong, X.; Heeger, A. J. *Adv. Mater.* **2006**, *18*, 572–576.
(42) Gilot, J.; Barbu, I.; Wienk, M. M.; Janssen, R. A. J. *Appl. Phys. Lett.* **2007**, *91*, 113520.
(43) Halls, J. J. M.; Pichler, K.; Friend, R. H.; Moratti, S. C.; Holmes, A. B. *Appl. Phys. Lett.* **1996**, *68*, 3120–3122.
(44) Markov, D. E.; Tanase, C.; Blom, P. W. M.; Wildeman, J. *Phys. Rev. B: Condens. Matter* **2005**, *72*, 045217.
(45) Brabec, C. J.; Zerza, G.; Cerullo, G.; Silvestri, S. D.; Luzzati, S.; Hummelen, J. C.; Sariciftci, S. *Chem. Phys. Lett.* **2001**, *340*, 232–236.

AM900660N